Large-Eddy Simulation of Transcritical Round Jets

T. Schmitt[1], A. Ruiz[1], L. Selle[2], B. Cuenot[1]

[1] *CERFACS, 42 Avenue G. Coriolis, 31057 Toulouse cedex, France*

[2] *IMFT, Institut de Mécanique des Fluides de Toulouse, Avenue C. Soula, 31400 Toulouse, France*

July 9, 2009

Abstract

In rocket engines, dense oxygen is injected in a high pressure environment, above its critical pressure. Oxygen temperature varies from a subcritical to a supercritical value. Thermodynamics, mixing and transport properties are no longer those of a perfect-gas mixture. The present study uses the Large Eddy Simulation code AVBP, developed at CERFACS to simulate such jets. Dense fluid flows are modelled by the use of a cubic equation of state, in conjunction with appropriate viscosity and thermal conductivity coefficients. A nitrogen round jet at supercritical pressure injected in a gaseous reservoir is simulated. Two cases are considered, one experiencing a transcritical injection (high-density injection), while the other one is injected at supercritical temperature (low-density injection). Mixing efficiency is studied and the stabilizing effect of the density gradients is identified. Results are in good agreement with available measurements. The funding for this research is provided by Snecma and CNES.

In rocket engines, dense oxygen is injected in a high pressure environment, typically above its critical pressure. Oxygen temperature varies from a subcritical to a supercritical value. In order to understand the physics of high-pressure flows in complex configurations, the development of a CFD code for predicting the flow features is of great interest and of great need, especially for long lasting development cycles as in the aerospace industry. For this reason Snecma, which is the prime contractor for European launcher Ariane 5 cryogenic propulsion systems and CNES (Centre National d'Etudes Spatiales), which is the government agency responsible for shaping and implementing France's space policy in Europe, have launched a program on the development of LES for supercritical combustion.

For a proper description of supercritical (SC) fluid dynamics, two major modifications must be made to the standard low-pressure Navier Stokes equations:

- An equation of state (EOS) that accounts for real-gas effects must be implemented.
- Transport models for mass and heat transfers must be modified.

These models (EOS and transport) are to be made consistent through the appropriate thermodynamic relations. The equation of state can be considered as the cornerstone of SC fluid modeling for it ensures the accuracy of the method in a quiescent fluid. Indeed, basic thermodynamic variables such as the density or the pressure dependence of the heat capacities are directly driven by the EOS. From a practical point of view, the equation of state must compromise between accuracy and computational cost, leading to cubic equations of state.

This paper is organized as follows : real-gas models are presented in Section 1, then the flow configuration and the numerical setup of the present simulation is presented in Section 2. Finally results are discussed in Section 3.

1 REAL GAS MODEL

In this section, two key ingredients of the numerical simulation of supercritical flows are presented: the equation of state (EOS) and the model for transport phenomena. In this work, the Peng-Robinson equation of state [1] was chosen for this work and has been implemented in the AVBP LES solver [2]. For a single species, it reads:

$$P = \frac{\rho r T}{1-b\rho} - \frac{\rho^2 a(T)}{1+2b\rho-b^2\rho^2} \tag{1}$$

where P is the pressure, T the temperature, ρ the density and $r = R/W$ with R being the perfect-gas constant and W the molar mass. The coefficients $a(T)$ and b are defined as:

$$a(T) = 0.457236\,\frac{(rT_c)^2}{P_c}\left[1 + c\left(1-\sqrt{\frac{T}{T_c}}\right)\right]^2 \tag{2}$$

$$b = 0.077796\,\frac{rT_c}{P_c} \tag{3}$$

where P_c is the critical pressure, T_c the critical temperature and the additional parameter c is defined as a function of the acentric factor ω_{ac} by:

$$c = 0.37464 + 1.54226\,\omega_{ac} - 0.26992\,\omega_{ac}^2 \tag{4}$$

Equation 1 is then used for a consistent derivation of the pressure dependence of thermodynamic coefficients (heat capacities, compressibility, speed of sound, etc.), as presented by Miller *et al.* [3], and the low-pressure reference is provided by the JANAF thermochemical tables [4]. The performance of this model for the present study is illustrated in Fig. 1 by comparing the density and the constant-pressure heat capacity C_p with data from

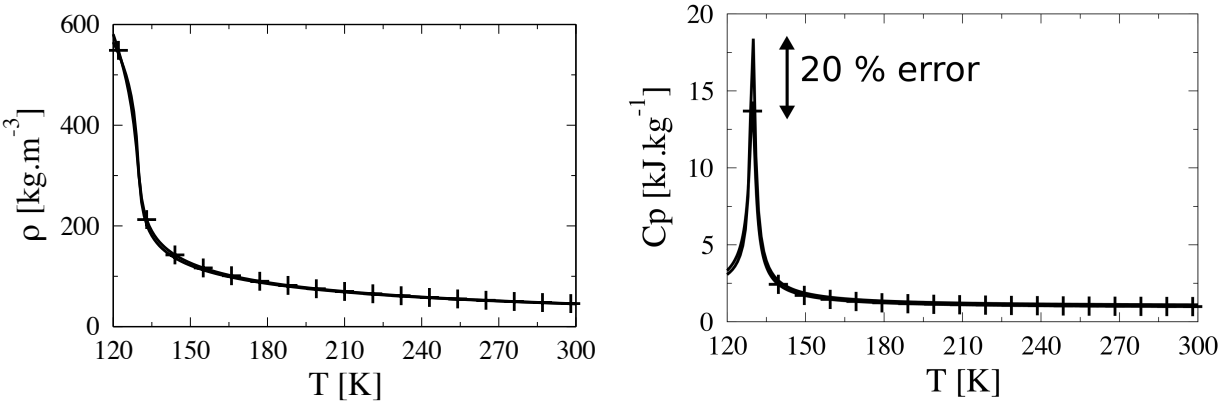

(a) Density

(b) Constant pressure heat capacity

Figure 1: Validation of the EOS and thermodynamics for N2 at 40 bars ($P_{c_{N2}} = 34\,bars$, $T_{c_{N2}} = 126\,K$) : —— NIST database; —+— real-gas model, based on the PR EOS [1]

the NIST database [5] at 40 bars and within the temperature range of the experimental conditions presented in Section 2.

The relative error is less than 3% for the density and 10% for the heat capacity, except near the pseudo-boiling line (c.f. Fig. 1 (b) around 130 K) where the error locally increases to 5% for the density and 20% for the heat capacity. The pseudo-boiling temperature T_{pb} is the temperature for which, at a given pressure, the constant-pressure heat capacity C_p reaches its maximum; it is the prolongation of the gas/liquid phase-change line.

Harstad and Bellan [6] proposed a formulation of transport phenomena under supercritical conditions consistent with kinetic theory at low-pressure. For the configuration considered in this work (c.f. Section 2), many simplifications can be made. Indeed, for single-species calculations, the only term that remains in the heat flux q_i is the classical Fickian contribution:

$$q_i = \lambda \frac{\partial T}{\partial x_i} \tag{5}$$

where λ is the thermal conductivity. The method proposed by Chung *et al.* [7] is used to compute the transport coefficients: the thermal conductivity and the dynamic viscosity μ. This method is based on the kinetic theory of gases, empirically corrected at high pressures.

These coefficients compare favorably with the NIST database within the thermodynamic conditions of this study (Fig. 2). Altogether, this model provides a quantitative evaluation of thermodynamic variables over a wide range of pressure (not shown here) and temperature. Noteworthy, it naturally degenerates toward perfect-gas behavior when the pressure is decreased.

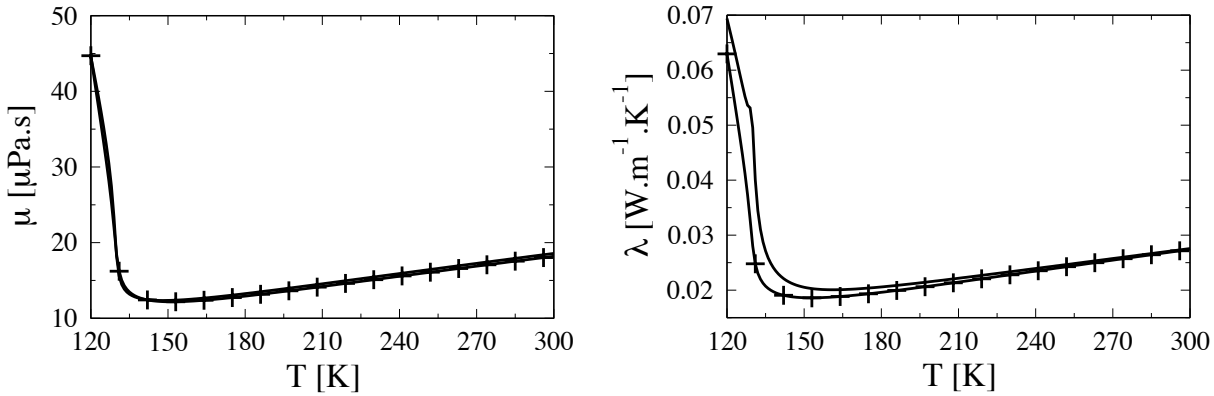

(a) Viscosity (b) Thermal Conductivity

Figure 2: Validation of the transport coefficients : —— NIST database; —+— Chung *et al.* [7]

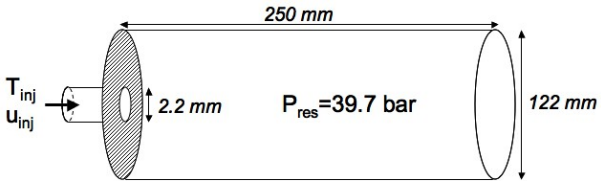

Figure 3: Sketch of the configuration

2 FLOW CONFIGURATION

The configuration for the numerical simulations is the experimental setup of Mayer *et al.* [8]. It consists of a single round jet (diameter 2.2 mm) injected in a cylindrical chamber (diameter 122 mm) pressurized at 39.7 bar at a temperature of 298 K (Fig. 3).

2.1 *Thermodynamic Conditions*

Two cases with a different inlet temperature were computed and are presented in Table 1. The two cases are numbered according to Mayer *et al.* [8].

Case 3 is a so-called «transcritical» injection: the injected fluid is evolving from a liquid-like state (high density) to a gas-like state (low density) after being heated up by

Case	T_{inj} [K]	$u_{inj}[m/s]$	T/T_{pb}	ρ_{inj}/ρ_∞	Re_{inj}
3	126.9	4.9	0.98	9.6	$1.7\,10^5$
4	137	5.4	1.06	3.7	$1.6\,10^5$

Table 1: Operating conditions for cases 3 and 4 of Mayer *et al.* [8]

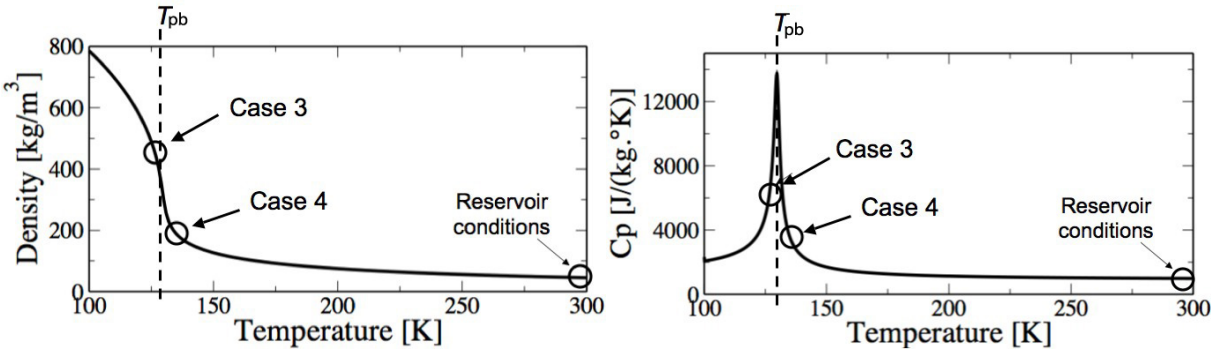

(a) Density (b) Constant-pressure heat capacity

Figure 4: Injection conditions for case 3 and case 4

the ambient hot gas. A large amount of energy is needed to change the jet temperature, as indicated in the C_p peak near the pseudo-boiling temperature T_{pb} in Fig. 4b.

The injection temperature of case 4 is very similar to case 3, however it is above the pseudo-boiling temperature ($T_{pb} = 129.5\,K$ at $39.7\,bar$ for nitrogen), which is reduces the difference with a perfect-gas case. Hence, case 4 is merely qualified as «supercritical» injection in the following.

Because of the strong changes in dynamic viscosity near the pseudo-boiling temperature (Fig. 2a), the Reynolds numbers at injection for cases 3 and 4 are very close: $Re_{inj} = 160\,000$.

2.2 *Numerical Setup: Mesh and Boundary Conditions*

A longitudinal cut of the mesh is displayed in Fig. 5a. The grid is finest near the injector, with a constant characteristic cell size of 0.1 mm over a distance of almost ten diameters. This zone is followed by a smoothly coarsening region. The mesh, which is the same for both cases, contains 950 000 points and 5 500 000 tetrahedra. The boundary conditions used in the present simulation are presented in Fig. 5b. The pressure in the reservoir is maintained by a non-reflecting outlet with a target pressure using the NSCBC technique [9] made consistent with the real-gas EOS [10]. The walls near the injector are treated as adiabatic while the reservoir walls are kept at a constant temperature of 298 K. The velocity and temperature are imposed at the inlet with turbulent perturbations prescribed by the procedure initially developed by Kraichnan [11, 12] and adapted to compressible flows [13] with an intensity of 2.5 % of the mean flow.

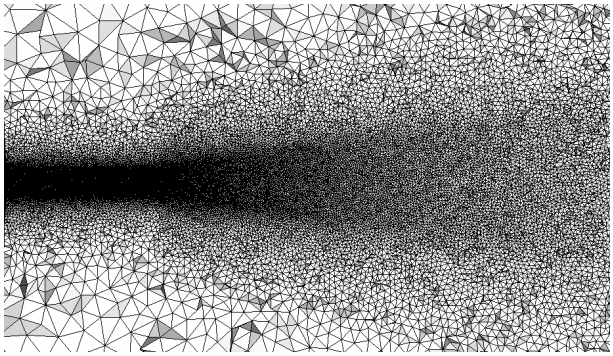

(a) Longitudinal cut of the computational domain's mesh on a length of 30 injector diameters

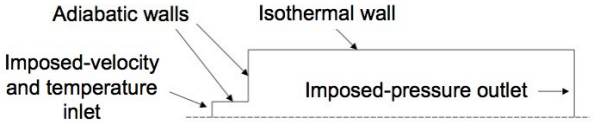

(b) Boundary conditions

Figure 5: Numerical setup

3 RESULTS

The centerline profile of density was experimentally measured by Mayer *et al.* [8] using 2D Raman technique. These results are compared with the present numerical simulations in Fig. 6. For case 3, the computational results accurately predict the drop in centerline density despite a small (10%) overestimation near the injector, which could be due to a systematic error of the Raman technique in very-high-density regions [8]. For case 4 however, experimental and numerical results differ notably. This could come from a small discrepancy between the simulation and the experiment injection temperature, which implies a very large discrepancy between injection densities, since the inlet thermodynamic state is very close to the pseudo-boiling point (cf. Fig. 4a). Finally, based on the centerline density profiles, one can evaluate the dense-core length x_{DC}, which is defined, in the present study, as the downstream distance from the injector, where the density decreases below 99% of its injection value. It is found to be 7.9 diameters for case 3 and reduces to 5.1 diameters for case 4.

In order to assess mixing efficiency, the initial destabilization of the dense-core and its transition to fully developed turbulence is studied. Fig. 8a shows the axial development of radial velocity perturbations u_r' in the shear layer. The development of u_r' in the near-injector region is much faster in case 4 than in case 3. In case 4, it reaches 20% of U_{inj} at 2 diameters, while it reaches 10% of U_{inj} at 13 diameters in case 3. An exponential fit of the initial growth of the velocity perturbation is made in order to obtain a spatial amplification coefficient k_i ($u_r' = y_0 + Aexp(k_i x/D)$). In case 4, k_i is approximately four times as high as case 3. The growth of the velocity perturbations appears similar to the Kelvin-Helmholtz instability and shows the stabilizing effect of the density gradient.

The effects of these velocity perturbations on the «dense fluid» is now investigated. The non-dimensional density ρ^+ is introduced:

$$\rho^+ = \frac{\rho - \rho_\infty}{\rho_{inj} - \rho_\infty} \tag{6}$$

When $\rho^+ = 1$, the fluid has the injection density. When $\rho^+ = 0$, it has the reservoir

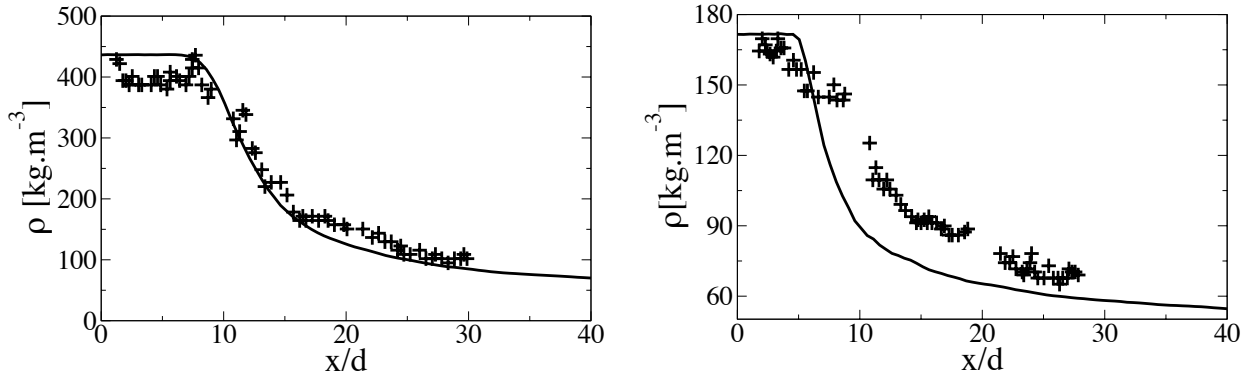

(a) Case 3 (b) Case 4

Figure 6: Comparison between experimental results and LES results of the centerline density in terms of normalized distance from the injector. —— present LES ; + Mayer *et al.* [8]

density. An isosurface at $\rho^+ = 0.5$ colored by velocity magnitude (the darker, the higher velocity) is shown in Fig. 7, and is here called the «dense fluid». The wrinkling of the dense fluid is then assessed isolating one-diameter-long slices and computing the surface to volume ratio of these slices. The instantaneous longitudinal evolution of the dense-fluid wrinkling is plotted in Fig. 8b . The wrinkling of the transcritical dense fluid is much lower than the supercritical one, which reduces the exchange surface between hot and cold fluid, *i.e.* heat transfer.

In order to identify the phenomena responsible for the increase of velocity perturbations, the enstrophy ω^2 balance equation is analysed

$$\begin{array}{rcccccc} \frac{D(\omega^2)}{Dt} & = & 2\underline{\omega}.(\underline{\omega}.\underline{\nabla})\underline{u} & -2(\underline{\nabla}.\underline{u})\omega^2 & -2\underline{\omega}.\frac{\nabla\rho\times\nabla P}{\rho^2} & +2\underline{\omega}.\underline{\nabla}\times(\frac{1}{\rho}\underline{\nabla}.\underline{\underline{\tau}}) \\ & & \textit{Stretching} & \textit{Dilatation} & \textit{Baroclinic torque} & \textit{Dissipation} \end{array} \quad (7)$$

where $\underline{\omega} = \underline{\nabla} \times \underline{U}$, $\underline{U}$ is the velocity and $\underline{\underline{\tau}}$ is the viscous stress tensor. The average non-dimensional source terms of the enstrophy equation are plotted in Fig. 9 for both cases. The radial profiles are taken at $x/x_{DC} = 0.5$ in order to get information about the dense-core destabilization. The total contribution of the source terms in Eq. 7 closely follows the profile of the baroclinic torque in both cases, showing the great importance of this term. Vortex stretching is approximately compensated by viscous dissipation. It appears that only the absolute value of the source terms are changed between case 3 and case 4 while their relative importance are approximately the same.

(a) Case 3

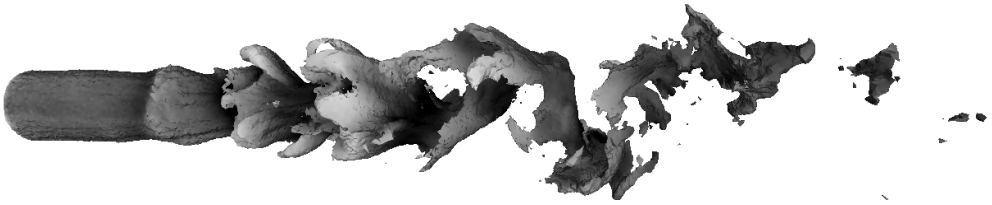

(b) Case 4

Figure 7: Isosurface at $\rho^+ = 0.5$ colored by velocity magnitude

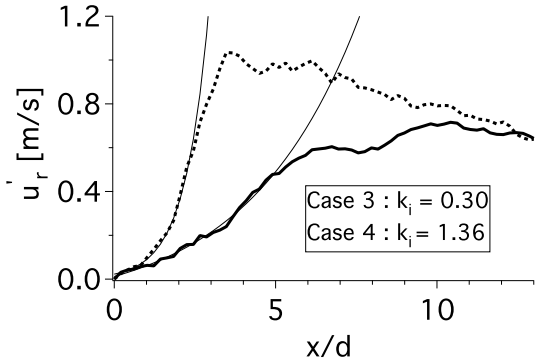

(a) Development of radial velocity perturbations. —— Case 3; ····· Case 4; —— exponential fits

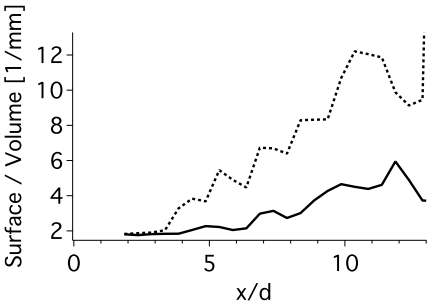

(b) Instantaneous wrinkling of the dense core. —— Case 3; ····· Case 4

Figure 8: Mixing efficiencies

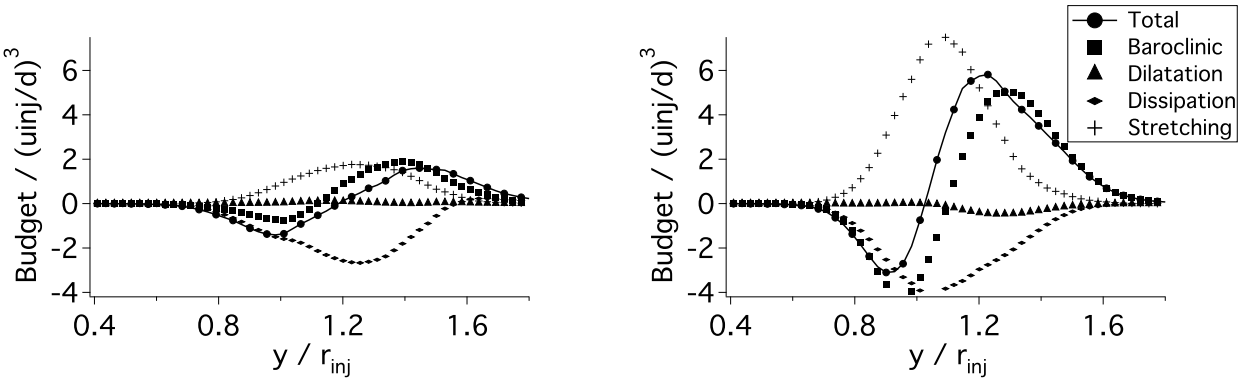

(a) Case 3, axial distance = 4 diameters

(b) Case 4, axial distance = 2.6 diameters

Figure 9: Enstrophy source terms in the transition zone of the two jets

4 CONCLUSION

A LES of a supercritical round jet representative of the dense-oxygen injection in rocket engines has been successfully undertaken. The dense-core length of case 3 is found to be much longer than case 4. The centerline density profile of case 3 is in very good agreement with the experimental results available [8] while case 4 shows discrepancies. The amplification rate of the radial velocity perturbations along the shear layer in case 3 is four times as low as case 4, which leads to delayed destabilization of the transcritical jet. The surface of the dense core in case 3 is shown to be much less wrinkled than case 4, which limits heat transfer.

References

[1] D. B. Robinson and D. Peng. A new two-constant equation of state. *Ind. Eng. Chem. Fundam.*, 15:59–64, 1976.

[2] T. Schönfeld and M. Rudgyard. Steady and unsteady flows simulations using the hybrid flow solver avbp. *AIAA Journal*, 37(11):1378–1385, 1999.

[3] R. S. Miller, K. G. Harstad, and J. Bellan. Direct numerical simulations of supercritical fluid mixing layers applied to heptane–nitrogen. *Journal of Fluid Mechanics*, 461(-1):411–412, 2002.

[4] *NIST-JANAF Thermochemical Tables*. National Institute of Standards and Technology, 1998.

[5] E. W. Lemmon, M. O. McLinden, and D.G. Friend. *Thermophysical Properties of Fluid Systems in NIST chemistry WebBook (http://webbook.nist.gov)*. National Institute of Standards and Technology.

[6] J. Bellan K. Harstad. An all-pressure fluid drop model applied to a bianry mixture: heptane in nitrogen. *International Journal of Multiphase Flow*, 26(10):1675–1706, October 2000.

[7] T. H. Chung, M. Ajlan, L. L. Lee, and K. E. Starling. Generalized multiparameter correlation for nonpolar and polar fluid transport properties. *Industrial and Engineering Chemistry Research*, 27(4):671–679, 1988.

[8] W. Mayer, J. Tellar, R. Branam, G. Schneider, and J. Hussong. Raman measurement of cryogenic injection at supercritical pressure. *Heat and Mass Transfer*, 39:709–719, 2003.

[9] T. Poinsot and S. Lele. Boundary conditions for direct simulations of compressible viscous flows. *Journal of Computational Physics*, 101(1):104–129, 1992.

[10] N. Okong'o and J. Bellan. Consistent boundary conditions for multicomponent real gas mixtures based on characteristic waves. *Journal of Computational Physics*, 176:330–344, 2002.

[11] R.H. Kraichnan. Diffusion by a random velocity field. *Physics of Fluids*, 13:22–31, 1970.

[12] A. Smirnov, S. Shi, and I. Celik. Random flow generation technique for large eddy simulations and particle-dynamics modeling. *Trans. ASME. Journal of Fluids Engineering*, 123:359–371, 2001.

[13] N. Guezennec and T. Poinsot. Acoustically non-reflecting and reflecting boundary conditions for injection of vortical flows in compressible solvers. *American Institute of Aeronautics and Astronautics Journal*, 2009.